Integration of Self-Lubrication and Near-Infrared Photothermogenesis for Excellent Anti-Icing/Deicing Performance

Xiangyu Yin, Yue Zhang, Daoai Wang, Zhilu Liu, Yupeng Liu, Xiaowei Pei, Bo Yu, and Feng Zhou**

The economic and safety issues caused by ice accretion have become more and more serious. Except for traditional ways of anti-icing, such as spraying agents, mechanical/thermal removal, etc., more economic approaches are urgently required. This work demonstrates the conceptual feasibility of using a self-lubricated photothermal coating for both anti-icing and deicing function. The coating is generally water repellent and infiltrated with hydrocarbon or perfluorocarbon oils as the lubricant to endow a liquid interface for preventing ice accumulation and minimizing the adhesion of ice on surfaces once it is formed. Fe_3O_4 nanoparticles are added to the film to afford high efficiency photothermal effect under near-infrared irradiation for rapidly melting the accumulated ice. The conceptual strategy can be easily implemented as a facile method to fabricate analogous sprayed coatings. It represents a major advance to tackle the challenging icing issue that is normally seen as a disaster in everyday life.

1. Introduction

The accumulation of ice on facilities may cause serious problems, such as the frozen rain disaster in southern China in 2008 and the snow disaster in northeast America in 2014,[1–5] by undermining the operational performance of aircrafts,[6,7] optical lenses,[8–10] energy transmission systems,[11,12] power lines,[3,13] wind turbines,[14,15] ships,[16] highways as well as building construction.[17–20] Therefore, anti-icing or deicing procedures have to be taken to alleviate the negative impact of icing. Among different approaches, spraying agents, usually polyol ether, that can lower the icing point is much popular, is mostly used, but is receiving more and more environment concerns. A large number of investigations have been conducted to understanding the icing mechanisms so as to look for alternative approaches.[5,21–26] The application of superhydrophobic materials to prevent ice formation by sliding or bouncing off water droplets before they are frozen has been frequently reported.[8,27–31] Indeed, the superhydrophobic material can effectively prevent ice formation at the initial stage of freezing or in a low humidity environment.[28,32–35] However, under high humidity conditions, moisture is liable to condense in the rough structure of superhydrophobic surface over time and once that happens, droplet will "grow" fast and finally freeze to form ice layer. As a result, the ice layer on superhydrophobic surface usually has much higher adhesion strength than that on smooth surface because it is more likely anchored onto the rough structures, which substantially makes it difficult to remove.[5,36–39] If moisture condensation in rough structure of water-repellent surface can be prevented, the icephobic ability would be greatly enhanced.[36,40–44] An alternative way for deicing is to reduce the adhesion and tensile strength between ice and substrate so that ice can be shaken off easily by natural force, such as wind, gravity, or vibration if the adhesion strength is even lower than 15 psi (100 kPa).[45,46] Hence, this type of material should be competent to prevent ice accumulation in winter storms. A new conception is reported that uses slippery liquid-infused porous surface (SLIPS) as promising icephobic material.[47–51] SLIPS presents a dynamic, molecularly smooth liquid interface with the capability of eliminating pinning points of droplets on it,[44,48] and reduces the adhesion in between since the traditional solid–ice contact is transferred to liquid–ice contact.

Now that not a real surface can perfectly prevent ice accumulation in humid and cold environment, a compromised way would be to delay the icing process and reduce ice-surface adhesion so that the ice can be removed easily.[52,53] The ice removal capability will further be enhanced with heating. To this end, the integration of SLIPS and thermogenesis into a single surface is arrived as a novel icephobic and deicing strategy. This will require heating methodology that can maximize the efficiency of external energy. Some of the nanoparticles (e.g., gold nanoparticles, carbon nanotubes, etc.) can perform the function since they can absorb specific stimuli for local heating.[54–56] Among different stimuli, laser is particularly attractive because

X. Yin, Y. Zhang, D. Wang, Z. Liu, Y. Liu, X. Pei, Dr. B. Yu, Prof. F. Zhou
State Key Laboratory of Solid Lubrication
Lanzhou Institute of Chemical Physics
Chinese Academy of Sciences
Lanzhou 730000, China
E-mail: yubo@licp.cas.cn; zhouf@licp.cas.cn
X. Yin, Y. Zhang
University of Chinese Academy of Sciences
Beijing 100049, China

DOI: 10.1002/adfm.201501101

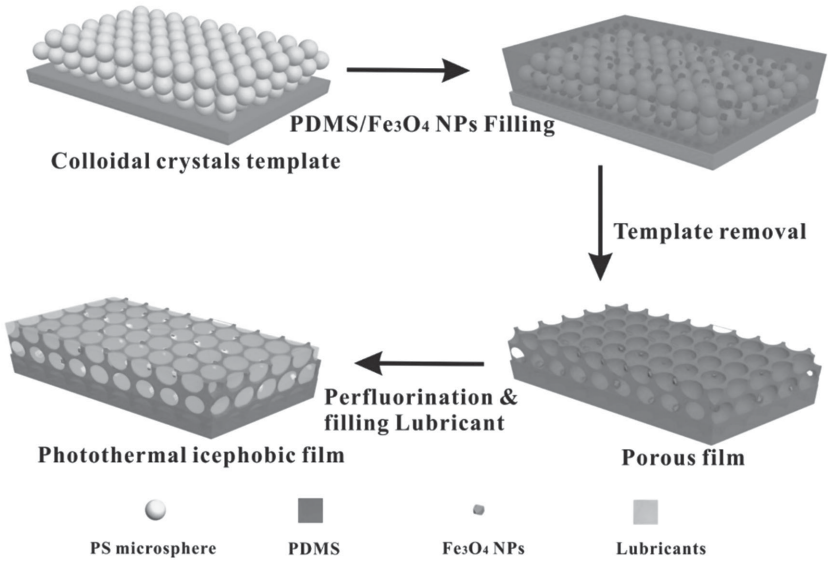

Scheme 1. Schematic procedures for fabricating photothermal icephobic film. It includes i) assembly of polystyrene microspheres onto substrate and used as the template; ii) pouring silicone precursor with Fe_3O_4 nanoparticles onto the template; iii) removal of PS sphere template; and iv) perfluorination with perfluorosilane and filling with perfluoro polyether lubricants.

of high energy density, high efficiency, easy handling, etc., and photothermogenesis has been used as triggers for controllable drug delivery, catalysis, and actuation, etc.[57,58] Fe_3O_4 magnetic nanoparticles (Fe_3O_4 NPs) have been verified with high thermogenesis efficiency by near-infrared (NIR) laser irradiation (an inexpensive and safe light source) for in vivo thermal therapy.[59,60] It is also highly promising for the laser-induced photothermal effect to be used for anti/deicing and meanwhile high penetration capability of NIR through heavy moisture and thick ice layer to reach the solid–ice interface is also required.[60] Therefore, in this paper we report the conceptual icephobic strategy by combining SLIPS and photothermal effect to delay ice accumulation and to remove ice easily.

2. Results and Discussions

2.1. Fabrication of Anti/Deicing Film

Scheme 1 shows the fabrication procedures of a model surface, which are experimentally simple. Typically, polystyrene (PS) microspheres are assembled into a compact opal crystal template, and then the Fe_3O_4 NPs-silicone precursor (Sylgard 184, Dow Corning) mixture solution is poured on the template. After solidification and removal of the template, an inverse opal porous PDMS (polydimethylsiloxane) film with uniformly distributed Fe_3O_4 NPs is formed, and is infiltrated with perfluoro polyether lubricants after fluorination.

The PS colloidal crystals have uniform spherical shape and monodispersed size (≈400 nm). It forms hexagonal lattice structure upon assembly on surface and is compact, highly regular and less-defects/cracks even in a relative large scale (**Figure 1**a and Figure S1, Supporting Information). After replicating the lattice structure, opaque PDMS film with 3D porous structure was obtained (Figure 1b). **Figure 2**c shows microscopic image of high-ordered reverse photonic crystals structure as a perfect replica of colloidal template. On the walls of each bowl-like structure, three micropores are left as replication of connected points of two colloidal crystals (Figure 1d). These structures exist both on the top and along the in-depth direction (Figure 1e). All pores are interconnected (Figure 1f), which

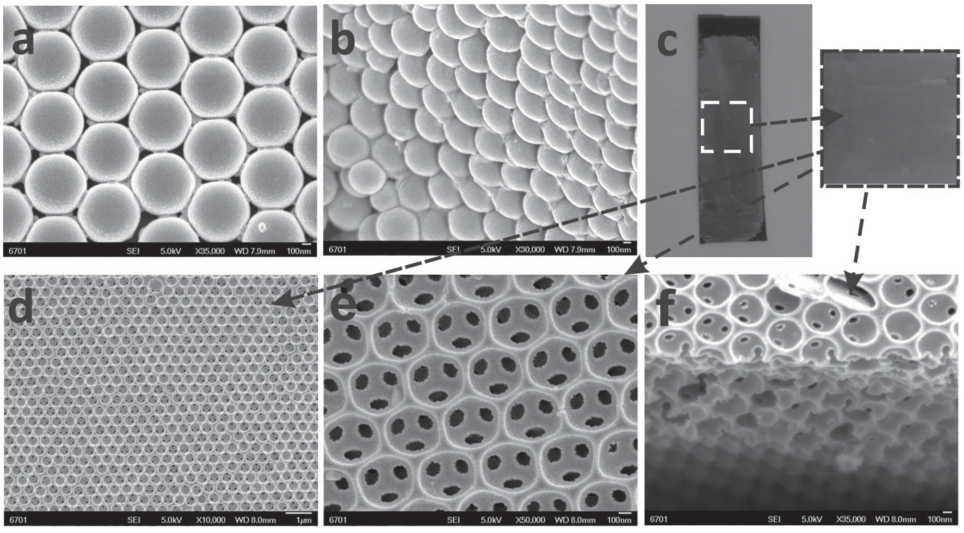

Figure 1. a,b) Microscopic images of polystyrene spheres and icephobic PDMS film. FESEM images of the top and cross-section view of PS colloidal crystals template. The PS spheres are closely packed both on top and along the in-depth direction. c) Optical photographs and d,e) FESEM images of as-prepared porous PDMS film on top and f) cross-section morphology, showing well replication of the inverse opal structure of the template.

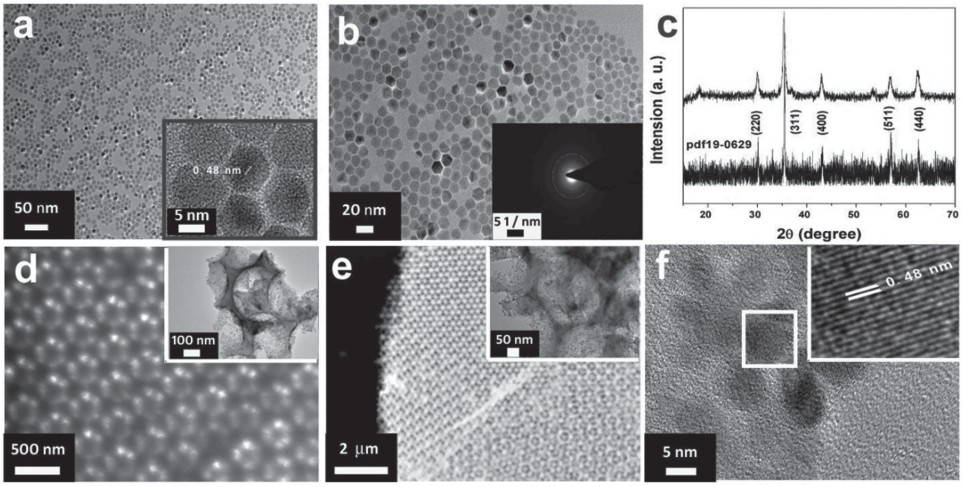

Figure 2. TEM images of Fe_3O_4 NPs and porous Fe_3O_4 NPs/PDMS. a,b) TEM images and c) XRD patterns of the as-prepared Fe_3O_4 NPs. Inset of (b) is the electron diffraction of Fe_3O_4 NPs. Insets of (a) and (f) are the corresponding high-magnification TEM images. d) TEM, e) STEM, and f) high-resolution TEM images of porous Fe_3O_4 NPs/PDMS film. Insets of (d) and (e) are the corresponding high-magnification TEM images.

provides reservoir to store lubricant and lubricant diffusion pathway.

For the purpose of deicing by thermogenesis, the oil-soluble Fe_3O_4 NPs are engineered into surface coating. The monodispersed Fe_3O_4 NPs have an average particle size of about 12 nm, which is consistent with the value (≈12.5 nm) calculated from the broadened peaks in X-ray diffraction (XRD) pattern according to the Debye–Scherrer equation (Figure 2a–c). XRD patterns of the nanoparticles match very well to the standard spinel phase of Fe_3O_4 with a lattice constant α = 8.41 Å (PDF 19-0629).[61–64] It has excellent dispersion in many nonpolar solvents and keeps stable even for several months, also in PDMS precursor and so in PDMS films. Transmission electron microscopy (TEM) analysis verifies very well dispersity of Fe_3O_4 NPs in high-ordered porous PDMS film (Figure 2d,e). In the inset of Figure 2a, the Fe_3O_4 NPs are all structurally uniform with an interplanar spacing about 0.48 nm, as indicated clearly from atomic lattice fringes, which corresponds to the (111) lattice plane of cubic Fe_3O_4 NPs (0.483 nm).[62] Similarly, the same atomic lattice fringes were also found in the as-prepared film, which further verifies that the Fe_3O_4 NPs successfully existed in the porous PDMS film (Figure 2f).

In order to verify the function mechanism of the strategy, different PDMS film samples were prepared for control experiment, i.e., pure and smooth PDMS film without pores, fluorination and lubricant (SF), porous film (PF), fluorinated porous film (FF), and fluorinated porous film infiltrated with perfluoro polyether (Krytox from Dupont) lubricant (LF). The anti-icing performance of icephobic materials (especially for the initial stage of ice formation) closely relate to their surface wettability.[41,44] The PF has poor water repellency and water droplet wets on the surface instantaneously despite of the hydrophobic nature of PDMS. Water droplet is more like being sucked into pores due to the capillary force and so it will not be further considered as the icephobic material. Due to its good water repellency and smoothness (Figure S2, Supporting Information), SF was adopted in this paper as an important reference to confirm the icephobicity of others. After fluorination (FF) with fluorosilane, it becomes superhydrophobic with water contact angle (WCA) above 150°, and the contact angle hysteresis is about 1°. When the porous film is filled with lubricant (LF), its WCA declines to about 85°, and this phenomenon is consistent to the correlative reports.[47,49] Despite of that, a defect-free and super-slippery surface is obtained due to the infiltration of liquid lubricant that can eliminate the moisture pinning defects, resulting in a small contact angle hysteresis (3° ± 1°).[49,50] All results mentioned above display a good water repellency of LF. Besides the water repellency, the adhesive force between water droplet and film is also an important measure to evaluate the anti-icing capability of icephobic film. It is seen from Figure S3 (Supporting Information) that the PF has the maximum adhesion force, and its water adhesive force is even larger than that on SF. The water adhesion force of FF is the smallest among all the tested samples because of the significantly reduced three phase contact area. The LF also exhibits a relatively small adhesion force. But different from FF, the reduction of adhesion on LF is caused by minimizing pinning points between the droplet and the solid surface.

2.2. Antifrost Property

The icephobic properties of the three films (FF, SF, and LF) were studied in two different simulated environment (frost, in low temperature, −10 °C, and high humidity environment, high humidity (RH) ≥70%, and freezing condition at low temperature, −5 °C, RH ≥70% and raining). All samples were mounted at a tilted angle of ≈60°. As reported previously,[37] the frost morphology on cold surface is time dependent, which subsequently has a great impact on the adhesion strength of frost with the surface. **Figure 3** presents the freezing process with time frost on different films. It is seen that frost was formed very soon (after 10 min) on SF and on FF as well (please note that the thin frost layer must have already changed the wetting property of FF). Frost formation on SF was much thicker than that on FF at the

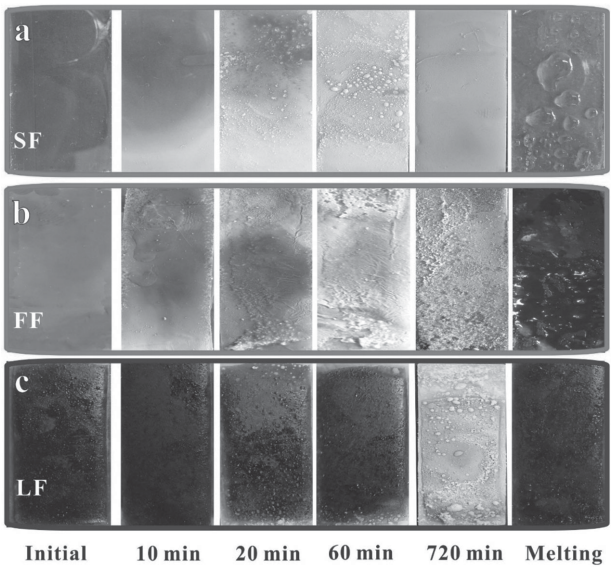

Figure 3. Frost formation with time and melting. Frost formation-removal images over time on a) SF, b) FF, and c) LF by deeply freezing under high humidity condition and subsequent deicing by photothermal effect. All samples were mounted with 60° tilt angle and a blue background was selected to highlight the contrast.

same time. After 60 min, very thick frost layer was formed on both SF and FF. However, there was no frost or ice on LF even at 60 min and only some sparsely dispersed frost appeared on the edge of this sample. All films were ultimately covered by frost after 12 h. However, the morphology of frost and its amount are completely different. The SF surface was fully covered with very thick, smooth, and compact ice layer, while frost on FF appeared as a large number of very fine grains with thick ice layer at the bottom and the ice layer was very rough with sparsely dispersed large frost grains on LF. These results suggest that moisture was easy to condense on SF, but the FF and LF significantly delayed condensation due to the different wetting property (WCA and WCA hysteresis).[30,32,65] However, over time, the water repellency and the antifrost property of FF disappeared because the moisture could condense into its micropores and displace pocket air inside film.[42,43,48] Upon freezing, ice would be much like being anchored onto FF surface. This imaginably makes ice on FF much harder to be removed. When the temperature was elevated to room temperature, frost became water droplets. Water droplets were heavily pinned on SF and even on FF, but easily slide off on LF, leaving no water droplets on it. The water droplet pinning on FF further proves that wetting transition occurred from metastable Cassie to Wenzel contact mode due to the penetration of water vapor into micropores, as the WCA became much smaller. Infiltration of lubricant into pores effectively prevents water vapor penetration. In a word, LF can not only delay frost formation, but also remove molten water much more easily than other films.

2.3. Defrost

The defrost property and the durability were quantitatively investigated by analysis of the frost adhesion strength on respective surfaces and were correlated to the WCA changes (**Table 1**). Counter intuitively, on FF surface, frost has the largest adhesive strength (>1700 kPa), the SF has the medium value (≈500 kPa), while the lowest adhesion strength (about 25 kPa) was found on LF. Thus, the frost on LF may be removed very easily with external disturbance.[48] FF has porous structure and the extremely high ice adhesive strength can be ascribed to the moisture condensation inside porous structure and so increase of contact area of ice with surface.[18,42] The moisture condensation can be verified with the significant WCA decline on FF from about 150° (before freezing) to about 67° (after defrosting), indicating the change of wetting mode from Cassie to Wenzel.[42] However, LF can maintain its water-repellent property very well (from about 85° to 83°).

Table 1. Water contact angles and frost adhesion strength on various surfaces.

Samples	Characteristics	WCA (before freezing)	WCA (after defrost)	Frost adhesive strength [kPa]
SF	Hydrophobicity	119° ± 5°	119° ± 5°	506.4 ± 27
FF	Superhydrophobicity	151° ± 4°	67° ± 2°	1758 ± 32
LF	Slippery	85° ± 3°	83° ± 2°	24.7 ± 5

The stability of lubricant is the key for its antifrost durability. In Figure S4 (Supporting Information), it is shown that the lubricant could take effect after more than 20 continuous freezing–defrost cycles or even longer.[51] We attribute its good durability to the high porosity in LF and immiscibility of perfluoropolyether lubricant with water in that the extremely large free volume of the porous PDMS allows high infiltration fraction of lubricant and meanwhile allows the easy lubricant migration to the top surface to maintain its antifrost property once the surface a spot of lubricant is lost in defrosting process and the immiscibility of lubricant with water can prevent it being flushed away by water.[51]

2.4. Anti-Icing

Apart from the frost accumulation, icing under freezing rain is more disruptive. Herein, the icephobic capabilities of the three samples were tested in simulated freezing rain environment: dripping condition (mimicking the raindrops, average ≈5 µL for each droplet, the impact height was set at about 10 cm) at −5 °C and the relative humidity above 70%. The icing speed was obviously accelerated compared with frost condition. From **Figure 4**, it is seen that the ice layers formed on all films in freezing rain environment are more compact and thicker than those formed under high humidity condition. Moreover, ice balls were clearly observed on LF, whereas compact, thick and densely packed ice layers formed on SF and FF. The reason is that water droplets impacting on rough FF surface at a certain speed tend to alter the wetting mode rapidly, while on LF wetting property is very stable.[5,42,65–67] In addition, the morphologies of the formed ice layer on films are closely related to their icing process and also have a great impact on the adhesion strength of ice on surface.[67] The ice layer adhesion strength on three different surfaces are all much higher than that formed

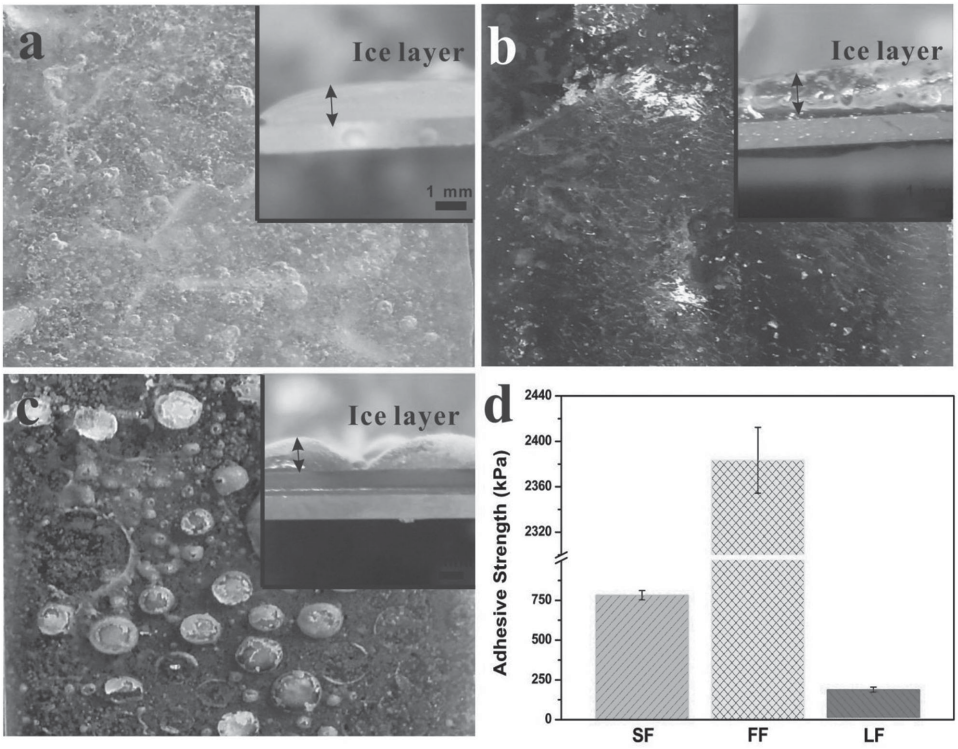

Figure 4. Ice formation and the adhesion characteristics. Digital images of ice layers formed on a) SF, b) FF, and c) LF under mimic freezing rain environment. d) The average ice adhesion strength on different films.

under humidity condition (Figure 4d), i.e., on FF, the ice adhesion strength reaches up to 2380 KPa, and above 100 kPa even on LF, which indicates that more extra force or thermal energy is needed to deice under freezing rain condition.

2.5. Deicing

The normal external disturbance, such as wind, gravity, or vibration is not enough to remove ice even on LF and ice removal must be assisted by outside force or heat. As schematically shown in **Figure 5**a, Fe_3O_4 NPs are used for photoresponsive thermogenesis. Figure 5b shows the temperature increase of FF with the irradiation time at ambient room temperature. Although the Fe_3O_4 NPs concentration in the film is very low (only 0.5 wt%), the surface temperature of LF increases obviously and exceeds 50 °C after only 10 s irradiation. It needs to point out that temperature increase at the coating surface is little affected by the surrounding temperatures in short time period since heat generation occurs only at the surface. On the

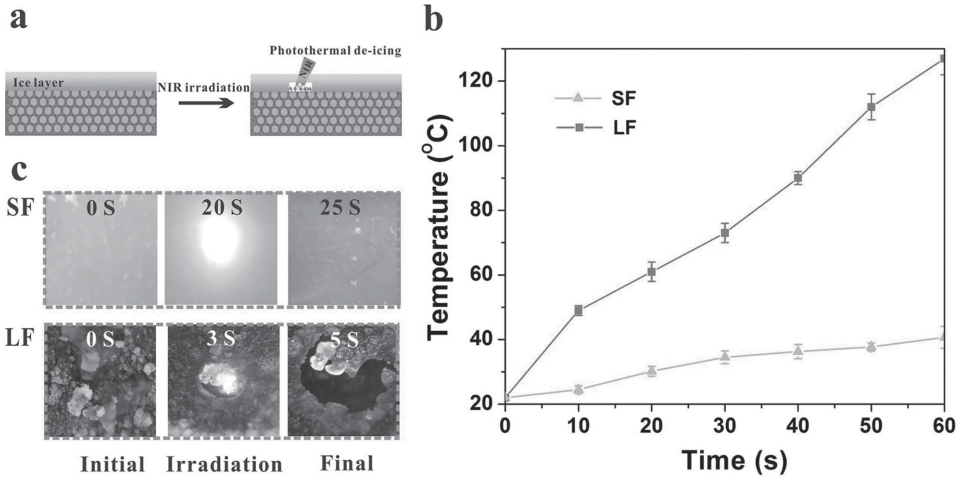

Figure 5. Laser-induced photothermal deicing. a) Schematic of the photothermal rapid deicing process. b) The plots of surface temperature with irradiation time at room temperature and c) the captured images from the deicing videos (Movies 1 and 2, Supporting Information), indicating ice melting process on SF and LF at different time.

contrary, even after 50 s irradiation, no obvious temperature change was detected on the nondoped film. It indicates that the icephobic film can generate heat to melt ice by laser irradiation in very short time. Although some temperature rise also exists on SF at room temperature, this cannot be found below 0 °C since the great thermolysis and relative low power laser irradiation.[58,59] Figure 5c shows that the ice layer formed under freezing rain condition (30 min) could be melted in 4 s even at simulated freezing environment below −5 °C. From the Movie 1 (Supporting Information), it is clearly seen that ice layer melt instantaneously with the movement of light spot. Water could slide off very quickly from the light shining area because of the good water repellency of LF. In contrast, the ice layer formed on the SF (nondoped) under the same condition did not melt even after 30 s irradiation (thermogenesis of NIR itself is weak, and it has no damage to the film, as shown in Movie 2, Supporting Information). The photothermal defrost process on SF and LF was given in Figure S5 (Supporting Information). Movie S3 (Supporting Information) shows frost on LF started to melt even after 2 s irradiation, while on SF only slight melting occurred from the outer frost due to the slight irradiation effect of NIR after at least 8 s (Figure S5, Supporting Information). It is evident that the melting process on the two films was fundamentally different: melting on LF started from the interface of ice and LF, demonstrating that the heat was generated from the film surface but not directly from the laser. While, slight ice/frost melting on SF started from outermost layer and needed a longer time due to the irradiation effect of NIR. Thus, we can safely conclude that the introduction of photothermal nanomaterial obviously benefits to ice removal by melting ice at the interface, which together with lubricating property of the surface plays a synergistic role in anti/deicing.

2.6. Photothermal Icephobic Engineering Coatings

Despite the effectiveness of the anti/deicing technique, the above surface fabrication process is costly, time consuming (several steps), and only applicable in small areas. For real applications, it is important to transfer the conception to a technology that is compatible with currently used engineering coatings that allow us to one-step fabricate photothermal icephobic coatings. For this purpose, we have used the liquid paraffin (LP) to replace both colloidal crystals template and perfluoro polyether lubricants to simplify the fabrication procedure. LP can be dispersed in the form of colloidal liquid drops in PDMS precursor and in cross-linked PDMS coating as lubricant. **Figure 6**a shows that the PDMS can be on-step spray-coated onto various substrate surfaces, such as Cu foil, Al foil, steel plate, PTFE plate, glass, etc. The method of pre-spraying an epoxy primer on substrate surface can enhance adhesive strength between the PDMS and the substrate surfaces, which is widely used to link the organic silicone coating with substrate for marine antifouling.[68,69] The microscopically morphology analysis of the sample after being extracted with petroether implies that the coatings also have porous structure that comes from the templating effect of LP (Figure 6c). The micropores are also the reservoir for LP. When the coating is very thin (about 50 μm), it is fully transparent irrespective of slight dark brown color. The sliding down of droplet on curved lens glass manifests the excellent water-repellency (WCA ≈83°, and low water contact angle hysteresis ≈3°) and the relative low formed frost adhesive strength (≈46 kPa).

Likewise, the LP-coating also has prominent photothermal icephobic property. Figure 4b shows the ice accumulation scenario on samples listed in Figure 6b (a half substrate was

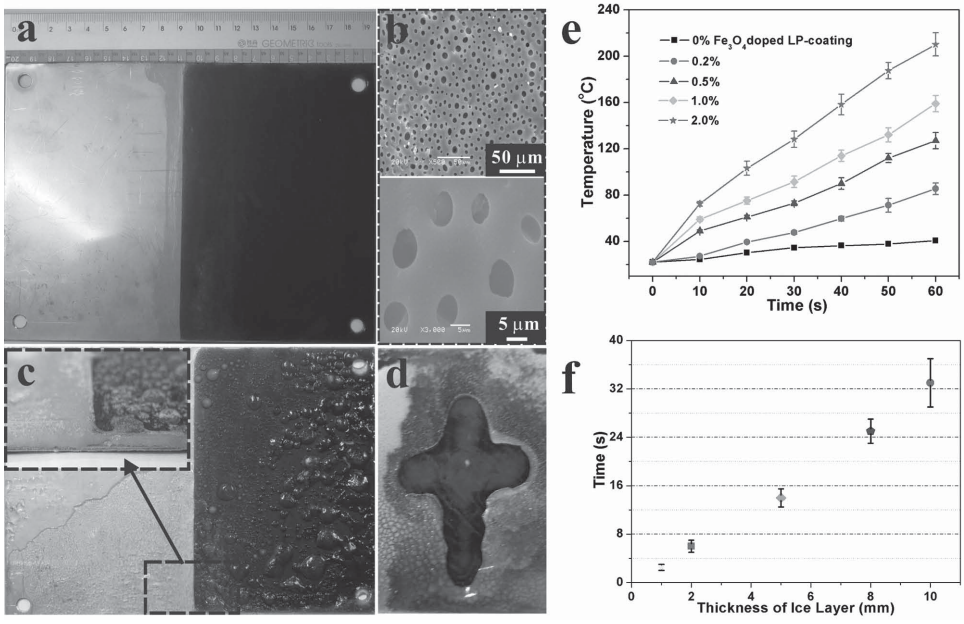

Figure 6. Spray-coated LP-coating and anti-icing property. a) The one-step fabricated LP-polyurea coating on steel plate. b) SEM images of LP-coating. It shows a large number of micropores are generated in the coating. c) Ice morphology of formed on LP-coating. d) The laser-induced photothermal burning of ice. e) Surface temperature change of LP-coatings with different nanoparticle dosage (0%, 0.2%, 0.5%, 1.0%, and 2.0%) under NIR irradiation. f) the thickness of ice layer versus irradiation time to melt on coating of 0.5% nanoparticle content.

coated with LP-coating). Compared with the blank side, all the coatings can delay ice accumulation effectively and ice has different loosely packed morphology. Indeed, the icephobic property of LP-coating is not as good as the perfluoro polyether, but the pothothermal technology makes up for it. It also enables the easy removal of the accumulated ice by photothermal effect and Figure 6d shows part of ice layer was burned away with short time NIR irradiation. The synthetic strategy of photothermal icephobic coating technically is feasible for large-scale production and applicable to surface icing protection of many base materials such as epoxy, polyurethane, acrylate, etc. The ice melting ability depends on both the laser light density and the concentration of Fe_3O_4 NPs in coatings, which can be optimized for applications in specific conditions. To better understand the influence of the Fe_3O_4 NPs concentration in coatings on the thermogenesis under NIR irradiation, we further measured the warming behavior of LP-coatings with different concentrations of Fe_3O_4 NPs (Figure 6e). It is clear that, by contrast to the virgin sample (no obvious warming is observed on the undoped coating), the temperature of the coatings with different Fe_3O_4 NPs doping amount increases obviously with NIR irradiation. Meanwhile, after the same irradiation time, the greater the doping amount is, the more obvious the temperature rises. Under the same irradiation intensity, the generated heat may accumulate with evolution of irradiation time. The melting time strongly depends on the time laser light to penetrate through ice layer. The quantitative relationship between the ice melting time and the thickness of ice layer on coating containing 0.5% nanoparticles is given in Figure 6f. It is shown that prolonging the irradiation time, more thick ice layer can be melted and a close to linear relationship between them was obtained. In summary, when LP-coating is exposed to NIR light, the Fe_3O_4 NPs work as a mass of microscopic heaters to rapidly and homogenously produce enough thermo energy to melt the ice layer.

3. Conclusions

In summary, a conceptual anti/deicing strategy is presented that combines the durable lubricating effect by infiltrating slippery liquid into porous surface and the photothermal effect afforded by Fe_3O_4 nanoparticles. The slippery liquid can be firmly locked in porous structures and forms a defect-free interface, which endows the film with stable and efficient water-repellency so that it can impede water vapor condensation and reduce ice adhesion strength. The uniformly dispersed Fe_3O_4 NPs in film can rapidly convert the optical energy of a NIR laser into thermal energy and thus endow the film with thermogenesis deicing capability in both high humidity and freezing rain environments. Moreover, NIR has better penetration ability through different materials, and so the ice, so it can be used for deicing in much complicated conditions where ice is formed in different morphology, transparency, etc. The optical approach also allows remote deicing. The photothermal icephobic conception can be very easily transformed from model surface to more industrial compatible engineering coatings technology for large-scale production. Although this work is still at its conceptual stage, the potential application prospect will inspire the design and fabrication of various next-generation anti/deicing materials, and is bound to promote the progress of the anti/deicing materials in practical application in future.

4. Experimental Section

Preparation of Porous PDMS Films: To prepare porous silicone film, the Fe_3O_4 nanoparticles solution was added to the mixture of PDMS prepolymer and curing agent (10:1, v/v, Fe_3O_4 NPs content 0.5 wt%). After stirring to form a uniform mixture, the mixture was spread on the PS colloidal crystals template (fabricated according to the reports 70, 71) to fill the void spaces among colloidal particles via capillary suction. It was then cured in an oven at 70 °C for 3 h. After curing, the Fe_3O_4-PDMS film elastomer was carefully peeled off from the mold and PS microspheres were selectively dissolved by immersing the film in a toluene bath for approximately 4–6 h. The porous PDMS film was fluorinated treatment by trichloro(1*H*,1*H*,2*H*,2*H*-perfluorooctyl)silane to form FF. 10 mL cm^{-2} Krytox 100 was infiltrated into fluorinated film by automatic wetting. Excess lubricant can be removed by drying with tissue paper.

Preparation of LP-Coating: The one-step fabrication LP-coating was prepared by utilizing LP as both lubricant and template. Typically, the mixture of PDMS prepolymer and curing agent (10:1 by weight), Fe_3O_4 NPs (0.5 wt%), LP, and hexane (mixture/LP/hexane: 25/20/55 (w/w/w) were blended uniformly and then sprayed on different substrates. After curing in an oven at 70 °C for 3 h, the LP-coating was obtained.

Characterization: The sample surfaces were observed by field emission scanning electron microscopy (FESEM, JSM-6701F, Japan) at 5 kV. TEM images, selected area electron diffraction (SAED), and energy dispersive spectroscopy (EDS) measurements were obtained on a TECNAI G2 TF20 high-resolution transmission electron microscopy under a working voltage of 200 kV (FEI, USA). The film was cut to ultrathin sections before the TEM analysis by a Leica EM FC7 ultramicrotome with a diamond knife at −120 °C cooled with liquid N_2. Powder XRD patterns were recorded on an X'Pert Pro Multipurpose diffractometer (PANalytical, Inc.) with Cu Kα radiation (0.15406 nm). The adhesion force of water droplets on different surfaces at room temperature were measured by a using a high-sensitivity dynamic contact angle measurement system (Data-Physics DCAT 11, Germany). Typically, about 10 mg water droplet was suspended with a metal ring first, and the substrate was placed on the balance table. The substrate was moved downward at a constant speed of 0.005 mm s^{-1}, until the substrate contacted the water droplet. The force increased and the shape of the oil droplet changed from spherical to elliptical. When the droplet was about to leave the substrate, the contact force sharply decreased, and the shape of the droplet changed back to spherical.

Icephobic Test: To observe their icephobic properties of different surfaces, all samples were monitored in homemade ice controllable equipment, which contains a custom refrigerator, a refrigerating box with observation window and a high sensitive temperature probe, and a controller system to adjust humidity and temperature. The whole icephobic tests are divided into four parts: antifrost, anti-icing, defrost, and deicing tests. During the antifrost tests, all the samples were placed in the controllable icing equipment with a tilted angle of ≈60° under a frost-forming condition (−10 ± 1 °C and RH = 70% ± 2%, kept for 720 min for all samples).[20,21,48] The antifrost data were regularly collected via a CCD camera. Additionally, the anti-icing tests that proceeded under the simulation freezing rain environment were also carried out in our controllable icing equipment. To mimic the rain droplets in nature, tiny droplets were sprayed onto the as-prepared samples via an array of microsyringe needle under −5 °C (mimic the raindrops, average ≈5 µL every droplet, the impact height of the droplets was set at about 10 cm).[44,67] All samples were kept in the mimic freezing rain environment for 120 min. The photothermal defrost and deicing tests were investigated in <−5 °C and RH ≈70% environment, where a near IR laser (808 nm, 1 W) was shone onto the as-prepared samples.

Ice Adhesion Strength Measurement: In this paper, the method of measuring the adhesion strength of ice was similar to widely used reports and gives a reproducible value of the ice adhesion of various surfaces.[48,66,67] The ice adhesion measurements were performed within the humidity-controlled chamber for the frost and defrost testing. All the ice adhesive strengths were averaged over 5 times measurements. The setup for measuring the ice adhesion strength consists of an XY motion stage, a custom force gauge which is from Wagner Instruments Force One FDIX with an accuracy of ±0.25 N), a home-built cooling stage, and water-filled cylindrical glass columns with a well-polished end (contact surface 1 cm^2) that were frozen onto the test surfaces. Then the cooling stage with the water-filled cylindrical columns atop of it was placed in a closed box. The test was carried out after the water (Milli-Q) in the cylindrical glass columns was kept at –15 °C for 4 h with high humidity, which ensured that water froze completely. The adhesive strength measurement of the ice formed in the mimic freezing rain environment is similar to the measurement for the high humidity, while, the only difference is that the samples are frozen beforehand in the mimic freezing rain environment. In addition, for the mimic freezing rain environment, the samples were first frozen for 1 h, and then were put to the water-filled cylindrical glass columns on the surface –15 °C for 4 h. Then the probe of the force gauge were derived to apply force by either pulling or pushing the sample columns to the ice columns via a syringe pump (Harvard Apparatus PhD Ultra) that was moved forward and backward at a rate of 0.5 mm s^{-1} and the peak force record required to detach each ice column.

Supporting Information

Supporting Information is available from the Wiley Online Library or from the author.

Acknowledgements

The authors thank NSFC (Grant Nos. 21303233, 51403220, and 21434009) for financial support.

Received: March 19, 2015
Revised: April 28, 2015
Published online: May 29, 2015

[1] A. K. Andersson, L. Chapman, *Accid. Anal. Prev.* **2011**, *43*, 284.
[2] H. A. Stone, *ACS Nano* **2012**, *6*, 6536.
[3] T. Li, J. Li, Electricity Distribution-Part1, 2009. CIRED 2009. *Electricity Distribution 20th International Conference and Exhibition on,* Prague, Czech Republic **2009**, p. 6.
[4] P. Guo, Y. M. Zheng, M. X. Wen, C. Song, Y. C. Lin, L. Jiang, *Adv. Mater.* **2012**, *24*, 2642.
[5] S. Jung, M. K. Tiwari, N. V. Doan, D. Poulikako, *Nat. Commun.* **2012**, *3*, 615.
[6] S. K Thomas, R. P. Cassoni, C. D. MacArthur, *J. Aircr.* **1996**, *33*, 841.
[7] J. Marwitz, M. Politovich, B. Bernstein, F. Ralph, P. Neiman, R. Ashenden, J. Bresch, *Bull. Am. Meteorol. Soc.* **1997**, *78*, 41.
[8] L. Mishchenko, B. Hatton, V. Bahadur, J. A. Taylor, T. Krupenkin, J. Aizenberg, *ACS Nano* **2010**, *4*, 7699.
[9] X. Yao, Y. Song, L. Jiang, *Adv. Mater.* **2011**, *23*, 719.
[10] J. Xiao, S. Chaudhuri, *Langmuir* **2012**, *28*, 4434.
[11] M. Farzaneh, *Atmospheric Icing of Power Networks*, Springer, New York **2008**.
[12] J. Y. Lv, Y. L. Song, L. Jiang, J. J. Wang, *ACS Nano* **2014**, *8*, 3152.
[13] J. L. Laforte, M. A. Allaire, J. Laflamme, *Atmos. Res.* **1998**, *46*, 14.
[14] N. Dalili, A. Edrisy, R. Carriveau, *Renewable Sustainable Energy Rev.* **2009**, *13*, 428.
[15] O. Parent, A. Ilinca, *Cold Reg. Sci. Technol.* **2011**, *65*, 88.
[16] M. Landy, A. Freiberger, *Nav. Eng. J.* **1968**, *80*, 63.
[17] L. Cao, A. K. Jones, V. K. Sikka, J. Wu, D. Gao, *Langmuir* **2009**, *25*, 12444.
[18] A. J. Meuler, G. H. McKinley, R. E. Cohen, *ACS Nano* **2010**, *4*, 7048.
[19] V. Alatyppö, K. Jutila, *XIII International Winter Road Congress*, Quebec, Canada **2010**, p. 2.
[20] L. B. Boinovich, A. M. Emelyanenko, V. K. Ivanov, A. S. Pashinin, *ACS Appl. Mater. Interfaces* **2013**, *5*, 2549.
[21] D. Ehre, E. Lavert, M. Lahav, I. Lubomirsky, *Science* **2010**, *327*, 672.
[22] S. Sastry, *Nature* **2005**, *438*, 746.
[23] Storm Water Technology Fact Sheet: Airplane Deicing Fluid Recovery Systems, EPA 832-F-99–043, U.S. Environmental Protection Agency, **1999**.
[24] Civil Aviation Authority of New Zealand. Aircraft Icing Handbook, Civil Aviation Authority (CAA), **2000**.
[25] A. C. Norrström, E. Bergstedt, *Water, Air, Soil Pollut.* **2001**, *127*, 281.
[26] M. Farzaneh, C. Volat, A. Leblond, *Anti-Icing and Deicing Techniques for Overhead Lines*, Springer, The Netherlands, **2008**.
[27] T. Sun, L. Feng, X. Gao, L. Jiang, *Acc. Chem. Res.* **2005**, *38*, 644.
[28] X. M. Li, D. Reinhoudt, M. Crego-Calama, *Chem. Soc. Rev.* **2007**, *36*, 1350.
[29] X. Deng, L. Mammen, H.-J. Butt, D. Vollmer, *Science* **2012**, *335*, 67.
[30] T.-S. Wong, T. Sun, L. Feng, J. Aizenberg, *MRS Bull.* **2013**, *38*, 366.
[31] L. Oberli, D. Caruso, C. Hall, M. Fabretto, P. J. Murphy, D. Evans, *Adv. Colloid. Interface. Sci.* **2014**, *210*, 47.
[32] D. Richard, D. Quéré, *Europhys. Lett.* **2000**, *50*, 769.
[33] Y. C. Jung, B. Bhushan, *Langmuir* **2008**, *24*, 6262.
[34] P. Tourkine, L. M. Merrer, D. Quéré, *Langmuir* **2009**, *25*, 7214.
[35] V. Bahadur, L. Mishchenko, B. Hatton, J. A. Taylor, J. Aizenberg, T. Krupenkin, *Langmuir* **2011**, *27*, 14143.
[36] A. Dotan, H. Dodiuk, C. Laforte, S. J. Kenig, *J. Adhes. Sci. Technol.* **2009**, *23*, 1907.
[37] S. A. Kulinich, S. Farhadi, K. Nose, X. W. Du, *Langmuir* **2011**, *27*, 25.
[38] J. Chen, J. Liu, M. He, K. Li, D. P. Cui, Q. L. Zhang, X. P. Zeng, Y. F. Zhang, J. J. Wang, Y. L. Song, *Appl. Phys. Lett.* **2012**, *101*, 111603.
[39] Li, K. S. Xu, W. X. Shi, M. He, H. L. Li, S. Z. Li, X. Zhou, J. J. Wang, Y. L. Song, *Langmuir* **2012**, *28*, 10749.
[40] S. A. Kulinich, M. Farzaneh, *Langmuir* **2009**, *25*, 8854.
[41] A. J. Meuler, J. D. Smith, K. K. Varanasi, J. M. Mabry, G. H. McKinley, R. E. Cohen, *ACS Appl. Mater. Interfaces* **2010**, *2*, 3100.
[42] M. Nosonovsky, V. Hejazi, *ACS Nano* **2012**, *6*, 8488.
[43] J. Chen, R. M. Dou, D. P. Cui, Q. L. Zhang, Y. F. Zhang, F. J. Xu, X. Zhou, J. J. Wang, Y. L. Song, L. Jiang, *ACS Appl. Mater. Interfaces* **2013**, *5*, 4026.
[44] L. Zhu, J. Xue, Y. Y. Wang, Q. M. Chen, J. F. Ding, Q. J. Wang, *ACS Appl. Mater. Interfaces* **2013**, *5*, 4053.
[45] S. Chernyy, M. Järn, K. Shimizu, A. Swerin, S. U. Pedersen, K. Daasbjerg, L. Makkonen, P. Claesson, J. Iruthayaraj, *ACS Appl. Mater. Interfaces* **2014**, *6*, 6487.
[46] R. R. Blackburn, B. J. Kinzig, C. G. Schmidt, *Strategic Highway Research Program,* National Research Council, Washington, DC **1993**.
[47] T.-S. Wong, S. H. Kang, S. K. Y. Tang, E. J. Smythe, B. D. Hatton, A. Grinthal, J. Aizenberg, *Nature* **2011**, *477*, 443.
[48] P. Kim, T.-S. Wong, J. Alvarenga, M. J. Kreder, W. E. Adorno-Martinez, J. Aizenberg, *ACS Nano* **2012**, *6*, 6569.
[49] R. A. Belisle, B. Hatton, T.-S. Wong, J. Aizenberg, *Nat. Commun.* **2013**, *4*, 2176.
[50] X. Yao, Y. H. Hu, A. Grinthal, T.-S. Wong, L. Mahadevan, J. Aizenberg, *Nat. Mater.* **2013**, *12*, 529.

[51] P. W. Wilson, W. Z. Lu, H. J. Xu, P. Kim, M. J. Kreder, J. Alvarenga, J. Aizenberg, *Phys. Chem. Chem. Phys.* **2013**, *9*, 581.
[52] J. Chen, Z. Luo, Q. Fan, J. Lv, J. Wang, *Small* **2014**, *10*, 4693.
[53] R. M. Dou, J. Chen, Y. F. Zhang, X. P. Wang, D. P. Cui, Y. L. Song, L. Jiang, J. J. Wang, *ACS Appl. Mater. Interfaces* **2014**, *6*, 6998.
[54] S. Nardecchia, D. Carriazo, M. L. Ferrer, M. C. Gutiérrez, F. Monte, *Chem. Soc. Rev.* **2013**, *42*, 794.
[55] Y. H. Li, G. Y. Huang, X. H. Zhang, B. Q. Li, Y. M. Chen, T. L. Lu, T. J. Lu, F. Xu, *Adv. Funct. Mater.* **2013**, *23*, 660.
[56] A. M. Gobin, M. H. Lee, N. J. Halas, W. D. James, R. A. Drezek, J. L. West, *Nano Lett.* **2007**, *7*, 1929.
[57] P. K. Jain, X. H. Huang, I. H. El-Sayed, M. A. El-Sayed, *Acc. Chem. Res.* **2008**, *41*, 1578.
[58] M. Q. Chu, Y. Shao, J. Peng, X. Dai, H. Li, Q. Wu, D. Shi, *Biomaterials* **2013**, *34*, 4078.
[59] C. H. Zhu, Y. Lu, J. F. Chen, S. H. Yu, *Small* **2014**, *10*, 2796.
[60] H. H. Richardson, Z. N. Hickman, A. O. Govorov, A. C. Thomas, W. Zhang, M. E. Kordesch, *Nano Lett.* **2006**, *6*, 783.
[61] H. P. Klug, L. E. Alexander, *X-ray Diffraction Procedures for Polycrystalline and Amorphous Materials,* John Wiley & Sons, New York **1962**.
[62] S. H. Sun, H. Zeng, D. B. Robinson, S. Raoux, P. M. Rice, S. X. Wang, G. X. Li, *J. Am. Chem. Soc.* **2004**, *126*, 273.
[63] T. Z. Yang, C. M. Shen, Z. A. Li, H. R. Zhang, C. W. Xiao, S. T. Chen, Z. C. Xu, D. X. Shi, J. Q. Li, H. J. Gao, *J. Phys. Chem. B* **2005**, *109*, 23233.
[64] S. F. Si, C. Li, X. Wang, D. Yu, Q. Peng, Y. D. Li, *Cryst. Growth Des.* **2005**, *5*, 391.
[65] J. C. Bird, R. Dhiman, H.-M. Kown, D. Quéré, *Nature* **2013**, *503*, 385.
[66] H. J. Wang, X. K. Xi, A. Kleinhammes, Y. Wu, *Science* **2008**, *322*, 80.
[67] K. K. Varanasi, T. Deng, J. D. Smith, M. Hsu, N. Bhate, *Appl. Phys. Lett.* **2010**, *97*, 234102.
[68] J. Stein, K. Truby, C. D. Wood, J. Stein, M. Gardner, G. Swain, C. Kavanagh, B. Kovach, M. Schultz, D. Wiebe, E. Holm, J. Montemarano, D. Wendt, C. Smith, A. Meyer. *Biofouling* **2003**, *19*, 71.
[69] J. Stein, K Truby, C. D. Wood, M. Takemori, M. Vallance, G. Swain, C. Kavanagh, B. Kovach, M. Schultz, D. Wiebe, E. Holm, J. Montemarano, D. Wendt, C. Smith, A. Meyer, *Biofouling* **2003**, *19*, 87.
[70] G. R. Yi, J. H. Moon, S.-M. Yang, *Chem. Mater.* **2001**, *13*, 2613.
[71] H. K. Choi, M. H. Kim, S. H. Im, O. O. Park, *Adv. Funct. Mater.* **2009**, *19*, 1594.